Comparative structural study of Al2O3–SiO2 glasses and amorphous thin films

Sirine Ben Khemis, Laurent Cormier, Ekaterina Burov, Hervé Montigaud, Benoit Baptiste, Sophie Nowak

Comparative Structural Study of Al_2O_3-SiO_2 Glasses and Amorphous Thin Films

Sirine Ben Khemis[1,2], Laurent Cormier[1], Ekaterina Burov[2], Hervé Montigaud[2], Benoit Baptiste[1], Sophie Nowak[3]

[1] *Sorbonne Université, Muséum National d'Histoire Naturelle, UMR CNRS 7590, IRD, Institut de Minéralogie, de Physique des Matériaux et de Cosmochimie, IMPMC, 75005 Paris, France*
[2] *Surface du Verre et Interfaces (UMR 125), CNRS/Saint-Gobain Research Paris, 93300 Aubervilliers, France*
[3] *Université Paris Cité, UMR CNRS 7086, ITODYS, 75013 Paris, France*

Corresponding author: L. Cormier, Sorbonne Université, IMPMC, cc115, 4 place Jussieu, 75005 Paris France

Email : laurent.cormier@sorbonne-universite.fr

Abstract

We compared the impact of alumina doping on the structure of Al_2O_3-SiO_2 amorphous thin films and bulk glasses using Raman spectroscopy and X-ray diffraction. In both thin films and bulk glasses, the addition of Al_2O_3 is accompanied by an increase in the mean Si-O-T angle and an evolution of the ring statistics with a decrease in the proportion of small rings. We evidenced structural differences between sputtered films and fused bulk glasses. Sputtered Al_2O_3-SiO_2 thin films are about 6-7% denser than their equivalent Al_2O_3-SiO_2 bulk glasses. This difference is mainly due to a change in ring statistics with the formation of small rings within the sputtered thin films. These structural differences in atomic structural organization highlight the impact of the synthesis conditions and open the door to further investigation of the structure-functional property relationships in sputtered Al_2O_3-SiO_2 thin films.

Keywords: Glass, Structure, Diffraction, Raman

1 INTRODUCTION

Non-crystalline (NC) materials can be prepared by a variety of processing routes that often leads to specific properties or structures.[1,2] Usually, a highly viscous liquid is rapidly cooled down, allowing for the elaboration of bulk glasses. Alternatively, NC thin films can be prepared through various methods, including chemical and physical vapor deposition (CVD and PVD), chemical reactions such as atomic layer deposition (ALD) or sol-gel methods. Amorphous films are scientifically and technologically important materials, with widespread applications due to their electrical, optical, magnetic or passivating barrier properties.

Among amorphous oxide thin films, SiO_2 and Al_2O_3 have received much attention given their applications as dielectrics or diffusion barriers.[3–7] When combined to form Al_2O_3-SiO_2 films, the properties change markedly up to 20 mol% Al_2O_3 while above this content there is a slow evolution towards those observed for the amorphous Al_2O_3 film.[8,9] The incorporation of aluminum ions, even at a low content, is likely to induce changes in the physico-chemical properties of silica and these changes are closely related to the evolution of the glass matrix structure. Therefore, a strong relationship between amorphous properties, composition and structural organization is expected and needs a detailed understanding to foster the optimization of new functional materials.

Though the SiO_2 film structure is very similar to that of silica glass,[7] subtle differences emerge from experimental studies. In both SiO_2 NC materials, short-range order (SRO) is essentially identical and corresponds to SiO_4 tetrahedra.[6,10,11] Each oxygen atom provides a corner-sharing linkage between two tetrahedra, forming a continuous random network, as originally described by Zachariasen[12] and further experimentally verified on 2D-films using atomically resolved Scanning Transmission Electron Microscope (STEM).[13] The rotational angle $\theta_{Si-O-Si}$ between Si-O bonds connecting two tetrahedra is a primary indicator of disorder. Since a very small energy is required to vary the θ angle,[14,15] there is a wide distribution of its value that yields the lack of long-range order (LRO) in both NC films and in silica.

The main structural differences between SiO_2 thin films and bulk silica concern the medium-range order (MRO) and the organization of the SiO_4 tetrahedra, which can be described by considering the ring size distribution. The network contains rings of varying sizes, the size *n* being given by the number of Si atoms. Ring statistics have been mostly inferred by Molecular Dynamics (MD) simulations.[16–21] For both films and bulk materials, about 80% of the ring distribution encompasses 5-, 6- and 7-fold membered rings, with a predominance of 6-membered rings (30-50%). The remaining distribution concerns smaller rings (12-18%) and larger rings (less than 10%). Recently, the analysis of the First Sharp Diffraction Peak in neutron structure factors has revealed a similar distribution.[22] STEM has also allowed a real space visualization of the 2D ring network in amorphous SiO_2.[13,23,24] Raman spectroscopy has been widely used to characterize the presence and proportion of small rings, i.e. four- (4-MR) and three-membered (3-MR) rings, as they give two sharp bands at 493 cm^{-1} (called D1) and at 602 cm^{-1} (called D2), respectively. Based on Raman analysis,[25,26] as well as simulations,[20] an excess of small membered rings has been revealed in thin films. In particular, D2 band intensities in NC films are typical to those observed in densified silica,[25,27,28] which is corroborated by higher density values in NC films compared to the bulk material.[7,25] Therefore, the structure of SiO_2 films differs from that of silica glass but is similar to that of densified silica. This densification affects the $\theta_{Si-O-Si}$ angle or the pair distances that can be determined in diffraction measurements (notably Si with O second neighbours, Si-O^{2nd}).[21, 23] Using the central-force model developed by Sen and Thorpe[29] and applied to the vibrational spectra of glasses by Galeener,[30] a relationship connects SiO_2 vibrations to $\theta_{Si-O-Si}$ and the force constant for the Si-O bond, $\alpha_{Si\text{-}O}$. From Raman or infrared spectra,[28, 31] a mean $\theta_{Si-O-Si}$ inter-tetrahedral angle of 141° is found for NC SiO_2 films compared to 144° for SiO_2 glass,[32, 33] consistent with a dense network in thin films.[25] Using grazing incidence X-ray diffraction (GI-XRD),[10] Si–O–Si bond angles were also determined for thermally grown SiO_2 films, with variations from 146.34° to 148.68°, indicating dependence on the fabrication process.

Contrary to SiO_2 that can readily form a glass, Al_2O_3 is reluctant to be vitrified from the liquid state and a pure Al_2O_3 bulk glass cannot be obtained, even using very high quenching rates.[34] Therefore, the structure of Al_2O_3 has only been investigated in thin films. The main structural point concerns the Al coordination environment, which was studied using ^{27}Al NMR,[5,

[35, 36] EELS (Electron Energy Loss Spectroscopy),[4] or X-ray diffraction.[37] Four-fold ($^{[4]}$Al) and five-fold ($^{[5]}$Al) coordinated Al are dominant (95%), while six-fold coordinated species ($^{[6]}$Al) are minor. The species distribution shows a pronounced similarity with predictions from MD simulations[38, 39] or experimental observations by diffraction [40] for Al_2O_3 melts. The fraction of $^{[5]}$Al depends on synthesis methods, with a higher fraction of $^{[5]}$Al in ALD than in PVD,[5, 41] and on the synthesis conditions, such as the deposition temperature or thickness.[42, 43] Though not uncommon to aluminosilicate glasses,[44–46] a high content of $^{[5]}$Al and $^{[6]}$Al is a major modification occurring in compressed glasses.[47–49] Their presence in Al_2O_3 films could arise from internal compressive stresses.[50] PDF analysis obtained from HE-XRD (High-Energy X-ray diffraction) has provided dynamic structural features suggesting the formation of an Al_2O_3 ALD coating surrounded by an O-rich surface layer.[51] Edge-sharing linkages occur between Al polyhedra due to the presence of high coordinated Al species and triply coordinated O species, $^{[3]}$O, whose proportion increases as the liquid is cooled down.[35,38,39] The significant contribution of edge-sharing of polyhedra is considered to increase liquid fragility,[39] thereby preventing the formation of a bulk Al_2O_3 glass.

In aluminosilicates, considering the difference between the Al-O and Si-O bond lengths (d_{Al-O} = 1.76 Å > d_{Si-O} = 1.62 Å),[52] the size of an AlO_4 tetrahedron is larger than that of a SiO_4 tetrahedron. Therefore, the substitution of Si by Al changes the network organization. Al_2O_3-SiO_2 films have been relatively understudied compared to their glass counterparts,[44] for which most of the structural studies involve compositions rich in alumina.[53–61] Al coordination in films prepared by rf sputtering with 3.2 to 87.1 mol% Al_2O_3 was investigated by Al Kα X-ray emission,[9] revealing that Al is primarily present in tetrahedral sites at low Al_2O_3 content (<1 wt % Al_2O_3).[59] As the Al_2O_3 content increases, the proportion of high coordinated Al sites increases. A similar trend is observed in Al_2O_3-SiO_2 glasses through numerous experimental investigations.[53–61] These studies have shown a majority of $^{[4]}$Al at low Al_2O_3 content, and more $^{[5]}$Al and $^{[6]}$Al species with increasing Al concentration. In binary aluminosilicates, the presence of $^{[4]}$Al species implies the formation of triclusters, O_T (an O bonded to three $(Si,Al)O_4$ tetrahedra), to ensure the charge compensation of $(AlO_4)^-$ units. However, these triclusters are overconnected species and yield an energetically unstable tetrahedral network. This explains that formation of high coordinated Al species will rapidly be predominant as Al_2O_3 content increases.[59] The aluminosilicate network contains Si-O-$^{[4,5]}$Al, Si-O-Si and Al-O-Al linkages with the absence of non-bridging oxygens. The addition of Al_2O_3 also changes the distribution of rings with small rings disappearing rapidly.[52,60]

The structure of binary aluminosilicate films is complex and remains poorly understood. In this paper, our study focuses on the impact of alumina doping on the evolution of the structure of thin films in comparison to that of bulk Al_2O_3-SiO_2 glasses. Emphasis will be placed on determining the atomic scale structure for both SRO and MRO using Raman spectroscopy and X-ray diffraction. These techniques make it possible to obtain structural information such as bond distance, bond angle and ring distribution, showcasing the dependence of these key parameters on composition or synthesis methods.

2 SAMPLE PREPARATION

2.1 Silica-based films

Pure and alumina-doped silica films were deposited by cathodic magnetron-sputtering at room temperature in reactive mode (0.2 Pa in Ar/O_2 plasma), as described previously.[25] The experimental parameters used for the deposition of the different films are summarized in Table 1. Before starting the process, the residual pressure of the deposition chamber was 10^{-5} Pa. A planar metallic target of silicon, undoped and doped with different Al contents, was pre-sputtered during 15 min to remove surface contamination and then deposition operates in pulsed direct current at a frequency of 100 kHz and 4.0 µsec off time. Substrates were scrolled under the Si:Al targets at a deposition rate of 0.045 $m.min^{-1}$ and at a power of 3000 W.

Silica-based layers of 150 nm and 600 nm were deposited on the atmospheric side of commercial soda-lime silicate glass (Planiclear®) for density and composition measurements. Additionally, layers of the same thicknesses were deposited on a glass substrate pre-coated with a stack of thin layers comprising the following sequence: SiO_2:Al(20 nm)/NiCr(2 nm)/Ag (50nm)/ZnO:Al(4nm). This thin layer stack is optimized to avoid silver oxidation during the

deposition step and thus to enhance its optical performances. Specifically, this stack is used as a "reflective mask substrate" that hides the glass substrate contribution in the Raman signal during thin layer acquisition. Table S1 presents the experimental parameters used for the deposition of the different films to prepare the "reflective mask substrate". Further details on the preparation of the "reflective mask substrate" and its efficiency for Raman analysis of thin films can be found in a previous paper.[25]

Table 2 provides the compositions of these sputtered films determined by ToF-SIMS. The name for each thin film is composed of the chemical symbol of aluminum and the mole content of Al_2O_3 (mol%) followed by "film" to refer to the thin film.

TABLE 1 Parameters used in direct current magnetron sputtering of Al_2O_3-SiO_2 thin films.

Target	**Si**	**Si:Al 95:5 (mol%)**	**Si:Al 81:19 (mol%)**
Thickness (nm)	150-600	150-600	150-600
Power (W)	3000	3000	3000
Pressure (Pa)	0.2	0.2	0.2
Ar flow (sccm)	20	20	20
O_2 flow (sccm)	24	24-34	24

2.2 Recovered silica-based films

With the aim of investigating the thin film structure by X-ray diffraction and avoiding any interference from the substrate signal, a film recovering method was developed to isolate the sputtered silica layer. For this purpose, the "reflective mask substrate", including a 50 nm thick silver layer, was used to host the silica films (600 nm). The sacrificial metallic Ag layer was dissolved by immersion in 6M reagent nitric acid, allowing the silica films to be floated off the solution. The details of the recovering process, ensuring no alteration of the film structure, were previously explained.[25]

2.3 Silica-based bulk glasses

Four Al_2O_3-SiO_2 bulk glasses were synthesized from Saint-Gobain by melting the mixture of oxide powders of industrial quality and quenching from high temperature above the melting temperature, giving homogeneous glasses, in the form of bars (5mm in diameter and several centimeters height), to be used as references. Samples were not annealed after quenching. Table 2 presents the compositions of these glasses determined by an electron probe microanalyzer (EPMA). Note that, contrary to cathodic magnetron-sputtering, it was not possible to obtain Al_2O_3-SiO_2 bulk glasses with high alumina content using the present fusion process, though contactless methods might allow synthesis up to 67 mol% Al_2O_3.[60] The glass name is composed of the chemical symbol of aluminum and the mole content of Al_2O_3 (mol%) followed by "bulk".

TABLE 2 Compositions of Al_2O_3-SiO_2 binary thin films determined by ToF-SIMS and their densities determined by X-ray Reflectometry. Al_2O_3-SiO_2 bulk glass compositions determined by EPMA and measured densities. The molar composition error in Al_2O_3 is 0.4 mol% for the bulk glasses, as estimated from the standard deviation of 10 points for each sample.

Composition	**Al_2O_3**		**Density (g cm^{-3})**
	%mol	**%weight**	
Al-0_{film}	0	0	2.35 ± 0.01
Al-3_{film}	3	5	2.38 ± 0.01
Al-19_{film}	18.6	28	2.50 ± 0.01
Al-0_{bulk}	0	0	2.218 ± 0.005
Al-1_{bulk}	1.18	2	2.243 ± 0.005
Al-2_{bulk}	2.4	4	2.250 ± 0.005
Al-5_{bulk}	4.87	8	2.276 ± 0.005

3 EXPERIMENTAL METHODS

3.1. In-depth composition

The compositions of the sputtered silica-based films (150 nm) on the glass substrate were

determined by ToF-SIMS (Time-of-Flight Secondary Ion Mass Spectrometry) depth profiling carried out using a TOF.SIMS 5 instrument (IONTOF, GmbH, Munster, Germany). A 25 keV pulsed Bi^+ ion beam, generated by a liquid metal ion gun, was used as the analysis beam, scanning a probed area of 100x100 μm^2, located in the center of the sputter crater (raster size = 400 x 400 μm^2). Sample erosion was performed by 20 keV oxygen cluster $(O_2)^n$ (n~1500, nominal size) generated by a Gas Cluster Source. The use of such sputter ions, combined with that of an electron flood gun, reduces surface charging effects that could induce alkali ions migration during the analysis. The depth profiles were acquired using the non-interlaced mode. The erosion rate was determined from the crater depth measurement (using a stylus profilometer), assuming a constant sputtering rate for the entire layer thickness. The elemental composition of the layer (Al, Si) was deduced from the intensity of corresponding secondary ions collected (Al^+, Si^+) and the calibration of these signals using standard samples.

Quantitative elemental analysis of the bulk glasses was performed by Electron Probe Micro Analysis (EPMA) using a Cameca SX100 (Ametek-Cameca, France) located at the CAMPARIS facility (Sorbonne Université, Paris, France), equipped with four wavelength-dispersive spectrometers. The measurements were performed with an electron beam at an accelerating potential of 15 kV and a beam current of 10 nA. The analysis was carried out at 10 different points on samples embedded in resin, then polished and recovered by a carbon coating. The compositions for the thin films and bulk glasses are reported in Table 2.

3.2. Thickness and density

Films thicknesses (150-600 nm) were measured with surface profilometry (Dektak XT, Bruker). An edge is created by partially masking the clean glass substrate before deposition and the mask is then removed with a cotton swab dipped in ethanol. In order to determine the effect of alumina doping on the density of silica films, we analyzed thin films (150 nm) with varying Al_2O_3 contents using the X-ray reflectometry (XRR) technique using a PANalytical Empyrean diffractometer (Amelo, Netherlands) with Cu Kα radiation. Figure S1 shows the X-ray reflectivity curves and Figure S2 shows the simulations allowing the determination of the densities, thicknesses and roughnesses that are summarized in Table 2 and Table S2.

The density of the different SiO_2-Al_2O_3 bulk samples was determined by the Archimedes flotation method using toluene as the immersion liquid. The densities for the thin films and bulk glasses are reported in Table 2.

3.3. X-ray diffraction

The X-ray diffraction (XRD) measurements were performed on a XCalibur S diffractometer (Agilent Technologies, USA) on powder samples filled in a kapton capillary with a diameter of 1.5 mm.[63] The 4-circle diffractometer is equipped with Mo $K\alpha_1$ radiation ($\lambda K\alpha_1$ = 0.709319 Å), operating at 50 kV and 40 mA, and data are collected with an Eos CDD detector. While the capillary was rotating on the phi axis, 2D images were recorded with increments of 2° (2θ), over the Q-range 0.3–15.9 $Å^{-1}$ (where the magnitude of the scattering vector, *Q*, is defined by $Q = 4\pi\sin\theta/\lambda$ with 2θ the scattering angle and λ the radiation wavelength). After subtracting the signal from the empty kapton capillary, the total structure factors, S(Q), were extracted using the PDFgetX3 code.[64] The Pair Distribution Function, PDF(r), was obtained after Fourier transform of the structure factor within the interval 0.8-15 $Å^{-1}$ using a Lorch function. This analysis was carried out on both the crushed Al_2O_3-SiO_2 bulk glasses and the Al_2O_3-SiO_2 recovered films.

3.4. Raman spectroscopy

Raman spectroscopy was performed in back-scattering geometry with a Renishaw® InVia™ Qontor® spectrometer having a solid-state green laser (532 nm) operating at an initial power of 50 mW. Spectra were recorded using a CCD detector (Peltier cooled charge-coupled device) in confocal configuration with a ×100 objective and grating with 2400 lines per mm, offering a spectral resolution of 1.2 cm^{-1}. An analyzed volume of ~1 μm^3 was determined from the instrument configuration. Spectra were acquired within a range of 100 to 1350 cm^{-1}. The lower Raman shift cannot be reached with the filter used in this set-up configuration. The signal was corrected by removing cosmic rays using the Nearest Neighbor algorithm and subtracting a baseline correction (more details on this correction can be found in the Supplementary

materials and Figure S3). To exclusively record the characteristic Raman spectrum of the silica film and eliminate the glass substrate signal, the analyses were carried out on the films deposited on the "reflective mask substrate".[25] To confirm the spectral homogeneity of the samples, Raman mapping scans were performed, and averaged spectra were retained. For a consistent Raman collection volume, an autofocus device (LiveTrack) was used to continuously adjust the height of the motorized microscope stage to maintain perfect focus during scanning.

4 RESULTS

4.1. Density evolution

Figure 1 summarizes the evolution of the density as a function of alumina content for the thin films and the bulk glasses. The graph also includes additional values obtained from the literature corresponding to Al_2O_3-rich silica glasses.[52,63] We observe a linear increase in density with the concentration of Al_2O_3 for both glasses and thin films, consistent with findings from previous studies on Al_2O_3-SiO_2 glasses with higher Al_2O_3 contents.[51,52,63,64] A recent study reports slightly lower density values for binary glasses with Al_2O_3 contents ranging from 0 to 7 mol% but these differences could result from different sample preparation as sintering at high temperature was used for their synthesis.[62] In addition, for equivalent concentrations of Al_2O_3, thin film layers are always denser than bulk glasses. This is explained by the characteristic densification effect under deposition condition using cathodic magnetron-sputtering.[25] Considering the density points of the binary glasses from the literature, presented in green in Figure 1, the degree of densification of the thin film layers remains constant compared to the equivalent bulk glasses, at least up to 19 mol% Al_2O_3. This observation indicates that the impact of Al_2O_3 on densification is similar in both thin films and bulk glasses.

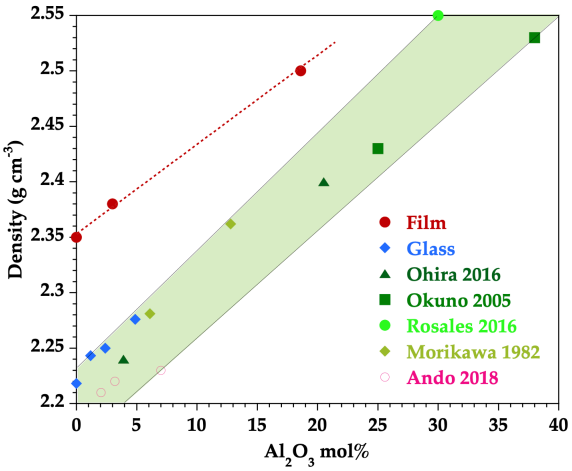

FIGURE 1 Evolution of the density for the thin film layers (red) and the bulk glasses (blue) as a function of Al_2O_3 content. The green symbols are previously reported values,[53, 54, 65, 66] showing the linearity in the density evolution up to high Al_2O_3 contents. The data (pink circles) from Ando et al.[62] are lower which could result from different synthesis conditions. Lines are guide for the eyes.

4.2. Raman spectroscopy

In Figure 2, the Raman spectra of thin film samples are compared with those of bulk glasses containing varying alumina contents. Due to the high concentration of SiO_2, the Raman spectra of the SiO_2-Al_2O_3 bulk samples are similar to pure silica (Al-0_{bulk}, red curve in Figure 2a), except in the 1000-1200 cm^{-1} range.

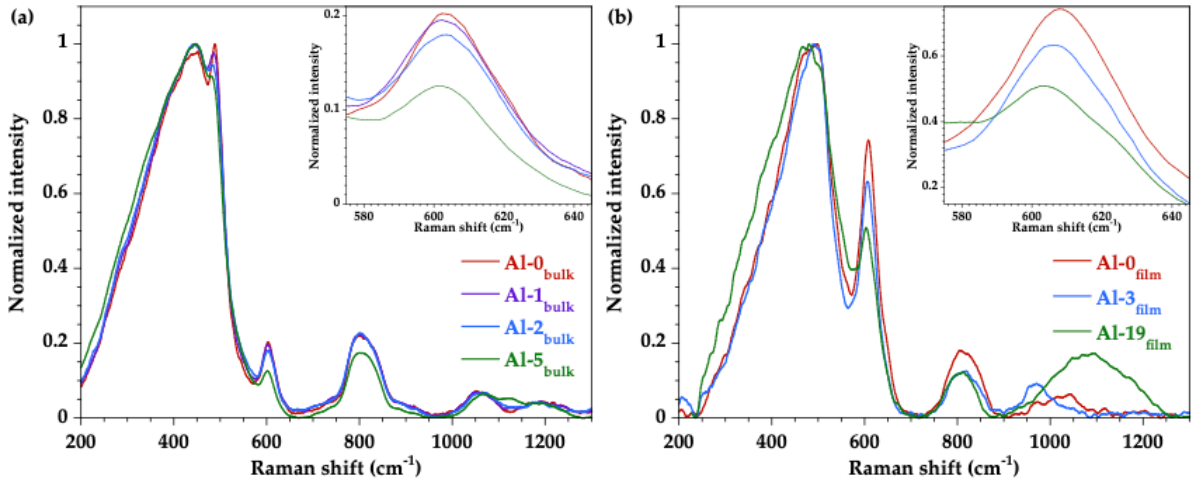

FIGURE 2 Raman spectra for (a) bulk glasses and (b) amorphous thin films containing different Al_2O_3 contents. In insert, zoom on the D2 bands to emphasize the variation in intensity.

At a low frequency ~475 ± 2 cm^{-1}, the position of the main band (MB) is dominated by bending vibrations of Si-O-Si bonds in large *n*-membered rings ($n \geq 5$) in silica.[67] This position remains nearly unchanged for the bulk glasses with low Al_2O_3 content. However, there is a slight broadening that reflects an increase in the distribution of T-O-T angles (T = Si or Al). The MB in thin films is characterized by a more marked evolution with the addition of Al_2O_3. As shown in Figure 3, the position of the maximum of this band, ω_{MB}, shifts towards lower frequencies. Initially localized at 490 cm^{-1} in the pure silica layer (Al-0_{film}), the MB position is shifted down to 480 cm^{-1} for 3 mol% Al_2O_3 content, and down to 470 cm^{-1} for 18.6 mol% Al_2O_3 content. This evolution reflects an increase in the mean inter-tetrahedral angle. We also notice a large broadening of the MB for the layer containing the highest content of Al_2O_3 (Al-19_{film}). This broadening reflects a significant distribution of T-O-T angles that could be due to the formation of large rings and a large distribution of highly coordinated Al species.

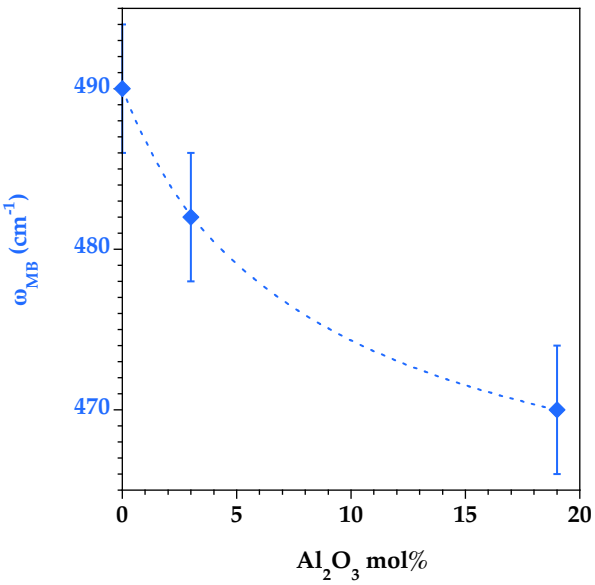

FIGURE 3 Evolution of the position of the main band, ω_{MB}, for the SiO_2-Al_2O_3 thin layers as a function of Al_2O_3 concentration. Lines are guide for the eye.

The bands D1 and D2 at 493 cm^{-1} and 602 cm^{-1} (inserts in Figure 2) are assigned to the breathing modes of four-membered (4-MR) and three-membered (3-MR) rings, respectively. These bands are more intense in the silica films than in the bulk glasses due to the increasing contribution of small rings and constraints in the dense sputtered films.[25] Compared with the intensities observed on pure silica glass, the intensities of the D1 and D2 bands decrease in the presence of Al_2O_3 for the bulk glasses and films. This reflects a

decrease in the proportion of small size rings with the addition of Al_2O_3, an observation consistent with previous studies on bulk glasses.[52,60]

The asymmetric band near 800 cm^{-1} results from the Si-O-Si bond stretching mode.[68] Its intensity slightly decreases and its position moves towards lower wavenumbers when adding Al_2O_3. This evolution may be associated with a decrease in Si-BO (Si-Bridging Oxygen) bond lengths.[69]

We also notice the appearance of a high frequency broad band (~1100 cm^{-1}) at high Al_2O_3 contents. This contribution is attributed to the symmetrical stretching vibration of a SiO_4 tetrahedron connected by vertices to three SiO_4 tetrahedra and one AlO_4 tetrahedron.[70] This presence indicates the incorporation of Al_2O_3 into the silicate network, forming interconnected Si-O-Al bonds at the expense of Si-O-Si ones.

For a more quantitative analysis of the Raman data, a fit of the spectra was carried out for all spectra in the spectral range 150-700 cm^{-1}, using pseudo-Voigt functions. The profile of this mathematical function includes four parameters: intensity, position, width at half maximum and Gaussian/Lorentzian ratio. Further details on the fitting procedure are available in the Supplementary Material. In the studied Raman range, a wide range of bending, rocking modes and their combinations are active. In previous investigations,[71] six functions have often been proposed for a decomposition of the MB. We consider that there is a systematic shift with ring size also for the alumina doped glasses and films and that the concentration for a given structure responsible for a Raman band is proportional to its area. Thus, by calculating the area of each contribution, we can estimate the proportion of the 4-MR and 3-MR constituting the structure. The proportion of the different contributions is then estimated by dividing the respective area by the total spectrum area between 200 and 700 cm^{-1}.

Figure 4 shows the fitting results of the Raman spectra measured on thin films with different Al_2O_3 contents, while the fit for the bulk glasses is presented in Figure S4. From the normalized area of each contribution, the evolution of the 4-MR (D1) and 3-MR (D2) proportions, as well as the MB structures impacted by the Al_2O_3 content, is presented in Figure 5a. The decrease in the D1 and D2 bands indicates that the number of small size rings decreases with the addition of Al_2O_3. Simultaneously, the contributions describing the main bands increase and these bands are associated with large size *n*-membered rings (n ≥ 5).[65,70] This trend (Figure 5b) is also observed for Al_2O_3-SiO_2 bulk glasses. These results are consistent with a previous study on binary glasses with a low Al_2O_3 content.[73]

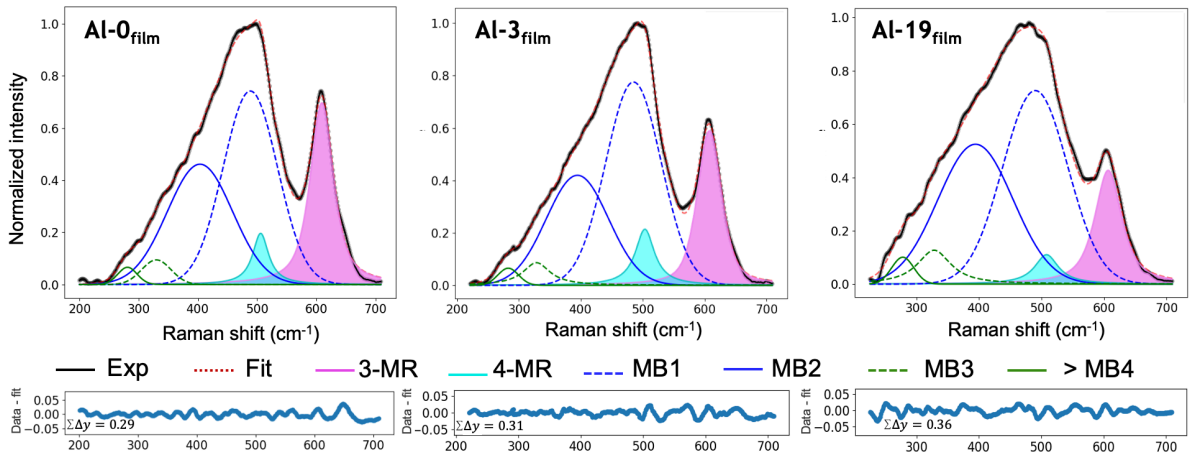

FIGURE 4 Fit of the Raman spectra for amorphous thin layers containing different Al_2O_3 contents.

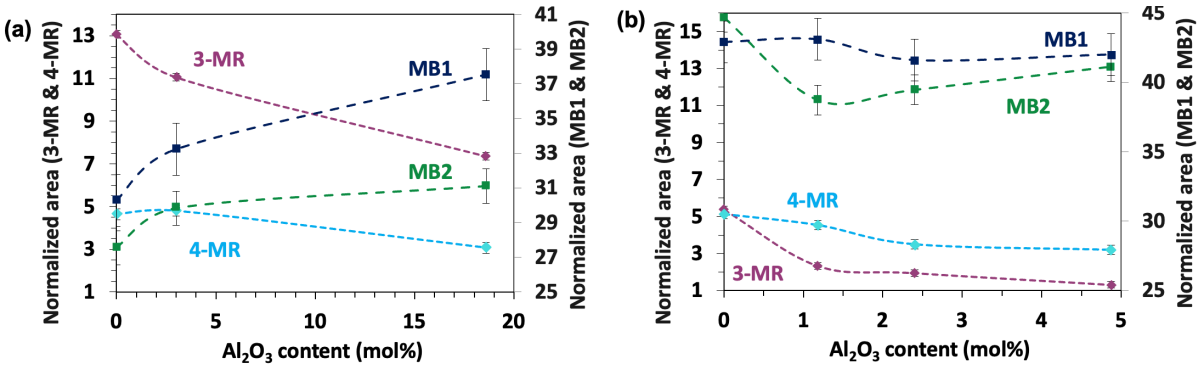

FIGURE 5 Evolution of the 4-MR and 3-MR proportions and the two main contributions (MB1 and MB2) for the band centered at ~490 cm^{-1} according to the Al_2O_3 concentration, resulting from the fitting results of the Raman spectra. (a) Thin films. (b) Bulk glasses. The 6-MR corresponds to the y-axis on the right.

4.3. Pair distribution functions

Binary Al_2O_3-SiO_2 bulk glasses are considered as references for interpreting the structural changes observed in thin films. The structure factors S(Q) for the four bulk glasses are plotted in Figure 6a. A similar S(Q) is observed for all the compositions, with a slight increase in the intensity of the first sharp diffraction peak (FSDP) with the addition of Al_2O_3, as shown in the insert in Figure 6a. This evolution is more pronounced in the richest Al_2O_3 sample (Al-5_{bulk}).

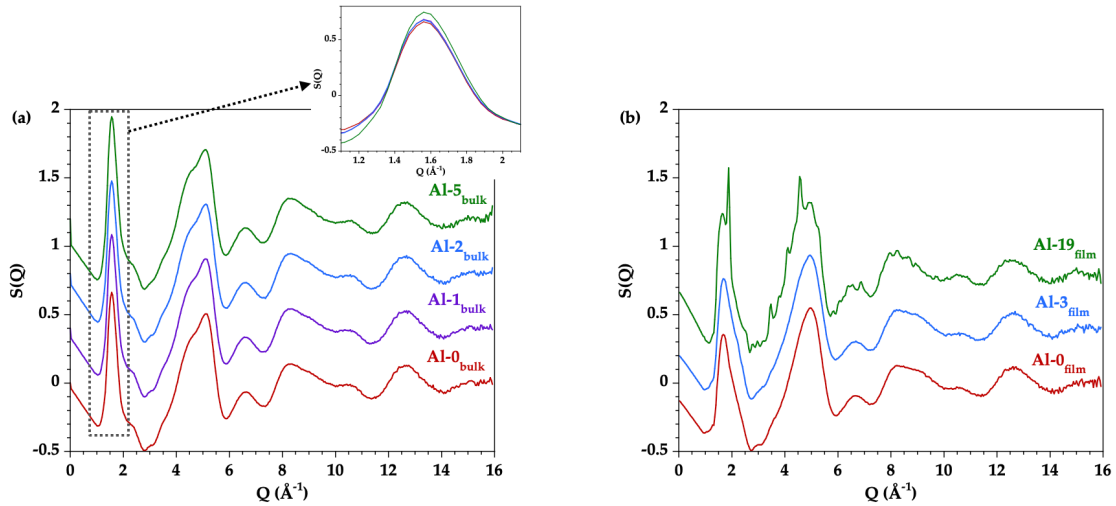

FIGURE 6 (a) Structure factors S(Q) of bulk glasses containing different Al_2O_3 content. The curves are drawn with an offset for better readability. In insert, the FSDP are represented to highlight the slight variation in intensity. (b) Structure factors S(Q) of thin film layers with different Al_2O_3 content. The curves are drawn with an offset for better readability.

Figure 7a shows the pair distribution functions (PDF) for the binary Al_2O_3-SiO_2 glasses obtained by Fourier transform of the S(Q) functions shown in Figure 6a. The lack of oscillations above 11 Å indicates the absence of long-range order, consistent with the amorphous nature of these materials. Six different pair contributions can be identified up to 6 Å, including T-O, O-O, T-T, T-O^{2nd} (O^{2nd} = O second neighbors), O-O^{2nd} and T-T^{2nd} (T^{2nd} = T second neighbors), based on literature.[51,52] Due to the low alumina concentrations, it is difficult to determine a clear evolution of interatomic distances. Indeed, the Si-O and Al-O distances are too close to be separated, so that a single peak, containing the two contributions, is observed. It has been previously shown that the first peak is shifted to higher *r* values with the addition of Al_2O_3.[50,72,73] The richest alumina glass (Al-5_{bulk}) is distinguished by a slight shift of the T-O peak, increasing from 1.61 Å to 1.62 Å (Figure S5a). This increase in the average T-O distance is due to a higher contribution of Al-O bonds, experimentally determined at ~1.76 Å in an AlO_4 tetrahedron, a greater distance than Si-O bonds at 1.62 Å in a SiO_4 tetrahedron.[52] The PDFs show a third peak that shifts from 3.08 Å in pure silica (Al-0_{bulk}) to 3.09 Å for Al-5_{bulk}

(Figure S5b). This distance corresponds to the T-T pairs, representing Si-Si, Si-Al and Al-Al.

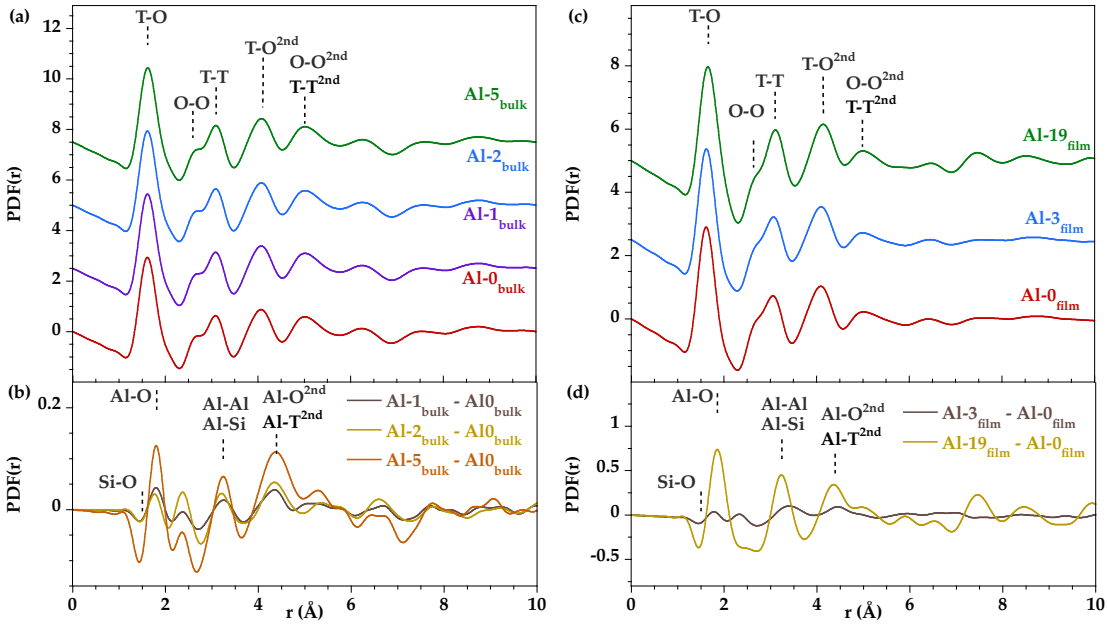

FIGURE 7 (a) PDF of SiO_2-Al_2O_3 bulk glasses containing different Al_2O_3 content. Curves are shifted with an offset for better readability. (b) Difference PDFs obtained by subtracting the data of Al-0b_{ulk} from each data of alumina-bearing glasses (Al-1$_{bulk}$, Al-2 $_{bulk}$, Al-5 $_{bulk}$). (c) PDF of SiO_2-Al_2O_3 thin layers with different Al_2O_3 contents. (d) Difference PDFs by subtracting Al-0$_{film}$ data from each of the alumina-bearing thin films data (Al-3$_{film}$ and Al-19$_{film}$).

To better understand the influence of low alumina contents and to probe the subtle evolution of interatomic distances, difference PDFs were obtained by subtracting data from pure silica (Al-0$_{bulk}$) from each dataset of the alumina-bearing glasses (Figure 7b). The positive contributions reflect those related to the addition of Al_2O_3. The first positive peak assigned to the Al-O pair is observed at a position varying between 1.78(1) - 1.80(1) Å. The intensity of this peak increases with Al_2O_3 content, reflecting an increase in the number of Al-O bonds. This peak shifts towards higher *r* values with the Al_2O_3 content, suggesting an increase in the Al-O distance. This evolution implies the potential presence of few highly coordinated Al species in five-fold ($^{[5]}$Al) and/or six-fold ($^{[6]}$Al) coordination. These species would have higher Al-O distances compared to those in AlO_4 tetrahedra ($^{[4]}$Al),[53,54,57] based on ionic size, where $^{[4]}$Al-O = 1.74 Å, $^{[5]}$Al-O = 1.83 Å, and $^{[6]}$Al-O = 1.88 Å.[76] The minority presence of $^{[5,6]}$Al in the sample with high Al_2O_3 content (Al-5$_{bulk}$) is further confirmed by a ^{27}Al NMR analysis that will be presented in a forthcoming paper.

A negative peak between 2.64-2.78 Å is attributed to the O-O bonds. This negative contribution is related to the decrease in the height of the O-O peak, which may result from the broadening of the O-O distance distribution due to the mixing of the Si-O and Al-O bonds. In addition, a positive peak is observed between 3.18-3.25 Å, with an intensity increase as Al_2O_3 is added The position of this peak shifts to higher *r* values with increasing Al_2O_3 content, reflecting the contribution of Al-Si (3-3.1 Å) and Al-Al (3.25 Å) pairs.[77] Finally, it is also possible to separate the Al-O^{2nd} contribution at 4.39-4.46 Å from the fourth positive peak.

Figure 6b shows the structure factors for thin layers with different Al_2O_3 contents. The signal is similar for the different samples. However, we note the presence of Bragg peaks at 1.88, 3.44, 4.08 and 4.6 Å^{-1} in the alumina-rich layer (Al-19$_{film}$). These peaks indicate the presence of Al_2O_3 crystals (ICSD 60419 (PDF 77-2135)). Conversely, a GI-XRD analysis on Al-19$_{film}$ layer deposited directly on a glass substrate indicates the absence of any crystallization (Figure S6). This suggests that the layer (Al-19$_{film}$) may have evolved under the high energy X-ray incident beam during the extended measurement time required for PDF acquisition (6 h). A similar effect was observed previously for a binary glass with higher Al_2O_3 content (67 mol%).[60]

Figure 7c shows the PDFs for the three thin layers with different Al_2O_3 contents. Unlike the PDFs of the pure silica layer (Al-0$_{film}$) and of the weakly Al_2O_3-doped layer (Al-3$_{film}$), which

both presents weak oscillations at high *r* values, the PDF of the richest alumina layer (Al-19$_{film}$) shows oscillations even at long distances, indicating a high level of ordering at medium range distance for this layer. This effect can be explained by the crystallization revealed by the presence of Bragg peaks in the structure factor.

Similar to bulk glasses, the PDFs for the thin films include six pairs up to 6 Å: T-O, O-O, T-T, T-O^{2nd}, O-O^{2nd} and T-T^{2nd}. With the addition of Al_2O_3, the first peak, initially at 1.615(5) Å in Al-0$_{film}$, shifts to 1.620(5) Å in Al-3$_{film}$ and 1.658(5) Å in Al-19$_{film}$ (Figure S7a). This change is explained by the increase in the contribution of Al-O bonds, which are longer than Si-O ones. The T-O distances within the layers are in good agreement with the values estimated from the correlation relationship between T-O mean distances and the Al_2O_3/SiO_2 ratio proposed by Zotov *et al*.,[75] using the following equation (with Al_2O_3/SiO_2 the weight percent ratio):

$$r(T\text{-}O) = 1.616 + 0.0716 \frac{Al_2O_3}{SiO_2} \qquad 2$$

In addition, an increase in the T-T distance occurs with the addition of Al_2O_3 (Figure S7b). Initially at 3.06(1) Å in Al-0$_{film}$, the T-T distance shifts to 3.07(1) Å and 3.11(1) Å in the Al-3$_{film}$ and Al-19$_{film}$ layers, respectively. This is explained by the contribution of the Al-Al and/or Si-Al bonds that have a greater length than the Si-Si ones. The Al-19$_{film}$ layer is also characterized by an increase in the intensity of the third peak, confirming high medium range order.

Figure 7d shows the difference PDFs, obtained by subtracting data of the pure silica layer (Al-0film) from each dataset measured on alumina-bearing layers (Al-3$_{film}$ and Al-19$_{film}$). Positive peaks at 1.83(1), 3.21(1) and 4.36(2) Å can be assigned to Al-O, Al-Al and/or Si-Al and Al-O2nd contributions, respectively. Table 3 summarizes the main mean distances and the assignments of pairs associated with these distances. From the T-O and T-T distances, the evolution of the mean T-O-T angle can be estimated. Initially equal to 143.5° in Al-0$_{film}$, the T-O-T angle increases slightly and reaches a value of 143.64° and 143.96° in Al-3$_{film}$ and Al-19$_{film}$, respectively. The same trend was observed in Raman spectroscopy. Moreover, the mean angle values found from the interatomic distances determined by PDF differ from those estimated by the ST model, which takes into account the position of the MB of the Raman spectra. This difference is explained because the ST model applied to Raman spectra considers only the average angle in the large rings (>5) characteristic of the MB, while the T-T distance is averaged over all rings.

TABLE 3 Peak distances (Å) and assignments observed in PDFs of thin layers of silica with different alumina contents and in differential PDFs.

	T-O	**T-T**	**T-O^{2nd}**	**O-O^{2nd}**	**T-T^{2nd}**
Al-0$_{film}$	1.610(5)	3.082(5)	4.07(1)	5.00(5)	6.21(5)
Al-3$_{film}$	1.620(5)	3.07(1)	4.10(1)	4.95(5)	6.50(5)
Al-19$_{film}$	1.659(5)	3.11(1)	4.16(1)	4.97(5)	6.47(5)
Al-0$_{bulk}$	1.616(5)	3.06(1)	4.10(1)	5.05(5)	6.42(5)
Al-1$_{bulk}$	1.615(5)	3.084(5)	4.07(1)	5.00(5)	6.23(5)
Al-2$_{bulk}$	1.615(5)	3.087(5)	4.08(1)	5.00(5)	6.22(5)
Al-5$_{bulk}$	1.620(5)	3.087(5)	4.07(1)	5.02(5)	6.28(5)
	Al-O	**Al-T**	**Al-O^{2nd}**		
diff	1.80	3.23	4.37		

5 DISCUSSION

The comparative study between NC samples prepared as thin films or bulk makes it possible to determine a structural impact of Al and to highlight some significant structural differences, especially at MRO, associated with different processing conditions.

5.1. Influence of Al_2O_3 addition

The Raman analysis indicates that the influence of Al_2O_3 addition on the network structure of the thin layers follows the same trend observed for Al_2O_3-SiO_2 bulk glasses. However, the

extent of structural changes depends on the concentration of Al. Aluminum atoms are incorporated into the silicate network by the formation of Si-O-Al bonds, which mainly impact the ring statistics. Since small rings are energetically unstable, they tend to disappear with the addition of Al_2O_3, especially considering that replacing SiO_4 units by AlO_4 ones in rings with low diameter induces even more constraints. For NC films and bulk glasses, the decrease in intensity of the D2 and D1 bands proves that addition of Al_2O_3 and the decrease of the SiO_2 content preferentially impact small size rings, allowing the formation of larger ones. A similar effect was previously observed with the addition of germanium oxide to silica.[78] This evolution explains that the MB is broadened and shifted towards lower frequencies, as a result of the symmetrical bond stretching vibrations of the Si-O bonds constituting the large rings. In parallel, the average T-T distances increase, as expected in large rings.

An increase in the density with the addition of Al_2O_3 is observed (Figure 1). Several reasons could explain this behavior. Three-fold coordinated Al have been determined in MD simulations and these species could favor locally dense structures.[55] However, these low-coordinated Al species have not been observed using ^{27}Al NMR though they were detected by Electron Paramagnetic Resonance (EPR) at very low Al_2O_3 content (< 50ppm).[77,78] Another explanation is the formation of high coordinated Al species, associated with the formation of triply bonded oxygen atoms and edge- and face-sharing linkages between AlO_n polyhedral. All these structural features favor more compact structures. Similarly, the density of Al_2O_3, composed of AlO_6 octahedra, is higher than that of SiO_2, composed of SiO_4 tetrahedra.[81]

5.2. Structural differences between thin films and bulk glasses

SiO_2 films contain significant higher fractions of small rings compared to bulk glasses. Thin films appear more disordered, as their PDF functions show less pronounced oscillations at high r values (above r > 5 Å) compared to those for bulk glasses. The lower T-T pair distances in films compared to glasses are also consistent with smaller rings, as such rings will bridge closer the SiO_4 and AlO_n units and reduce the θ_{T-O-T} angle. Small rings are considered as topologically over-constrained and unstable,[82] and they correspond to small inter-tetrahedral T-O-T angles.

The large fractions of small rings at low Al_2O_3 concentrations suggest a locally dense, more efficient packing arrangement of TO_4 units in thin films compared to glasses, consistent with density and packing values (Figure 1 and Figure S8). A more compact structural organization was already observed for pure SiO_2 thin films compared to silica glass.[7,25,26,28] According to simulations, NC films result in high potential energy and high packing efficiency.[20]

The synthesis of bulk glasses at high temperatures allows for more relaxation of the structure and limits the formation of small rings. On the contrary, the vapor deposition conditions (fast rate, high energy ions bombardment) do not permit the system to explore a large configurational space and prevent the relaxation of the structure towards more stable configurations. As a result, NC films retain a large number of small rings in their structure.

PDF analyses indicate that the SRO is essentially identical between NC films and bulk glasses, as this organization range is governed by the strong Si-O and Al-O bond strengths. Small changes in Al coordination number will be hardly detectable at such low Al contents, contrary to NMR analysis. On the contrary, MRO captures significant differences with different synthesis conditions, as it is related to weaker and longer-range forces. Small variations in θ_{T-O-T} angles require few changes in energy,[14] that can impact MRO. Characterizing the MRO in disordered materials is then an important source of structural information, raising the possibility for a comprehensive understanding of structure-property relationships.

5.3. Origin for the dense structure in thin films

The densification and atomic structural organization within the silica thin films can be attributed to the high-energy ion bombardment during deposition, leading to an increase in film compactness. During the plasma process, energetic ions from the plasma collide with the film surface, inducing a physical bombardment of the backbone bonds.

The high-energy ion bombardment gives rise to the "atomic peening" process.[81,82] This conceptual model reflects the notion that, as the film grows, the bombardment by energetic particles involved in the spraying process forces some atoms to be incorporated into the material with an atomic density higher compared to the one obtained when quenching a liquid

to form a glass (Figure 8).

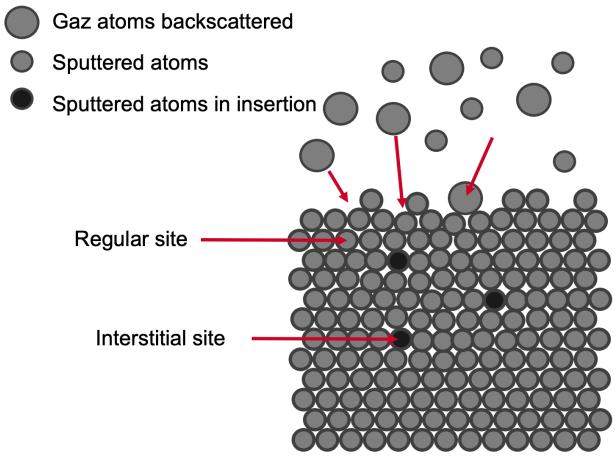

FIGURE 8 Schematic representation (adapted from Debelle)[85] of the «atomic peening» model where the growing film is bombarded by energetic particles (sputtered and backscattered atoms) during the sputtering process, which causes dilatation at the microscopic scale.

Previous studies have explored the occurrence of shear strain during compression, influencing silica densification.[86–90] Recent MD simulations and Raman spectroscopy studies have detailed how shear strain facilitates silica densification, promoting the formation of small rings at the expense of larger ones.[89,90] In the present work, the impact of ion bombardment energy on the proportion of small rings in the silica film is highlighted by the evolution of Raman features with increasing process pressure (Figure 9). As pressure deposition increases, the impinging ions energy decreases, resulting in a reduced peening effect on the depositing film by accelerated ions.[93] Figure 9 exhibits a pronounced evolution of the D2 band, assigned to 3-MR. A continuous decrease in the intensity of this band accompanies the increase in deposition pressure, indicating a reduction in the proportion of 3-MR. This behavior can be explained by gas scattering effects and the suppression of atomic peening. The increased pressure leads to more collisions in the gas phase in the path from the target to the substrate, increasing the angular distribution and reducing the kinetic energy of sputtered particles.[94]

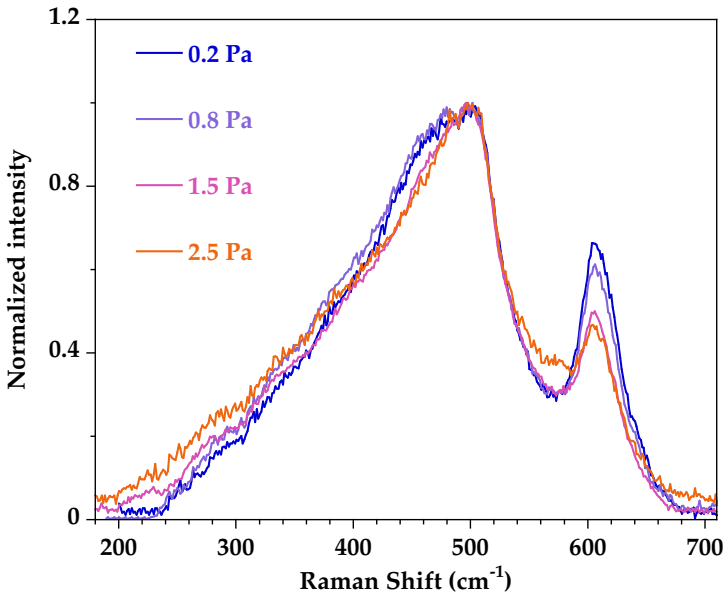

Figure 9 Raman spectra of thin silica films deposited at different process pressures on a glass substrate.

Hence, the significant increase in the proportion of small 3-MR observed in the thin layers in the present study is primarily attributed to the ion energy bombardment during film

deposition. This deposition condition constrains the system, limiting its exploration of a vast configurational space and impeding the relaxation of the structure toward more stable configurations. Consequently, NC films retain a considerable number of small rings in their structure. In contrast, the synthesis of bulk glasses at high temperatures allows for greater structural relaxation, thereby inhibiting the formation of small rings.

6 CONCLUSIONS

The structure of Al_2O_3-SiO_2 thin films synthesized by the magnetron sputtering deposition was investigated using X-ray diffraction and Raman spectroscopy, in comparison to that of bulk Al_2O_3-SiO_2 glasses. The impact of the synthesis conditions and the addition of Al_2O_3 on the atomic structural evolutions of the silicate network were investigated.

Structural differences between sputtered films and fused bulk glasses have been highlighted. We showed that the sputtered Al_2O_3-SiO_2 thin films are about 6-7% denser than their equivalent Al_2O_3-SiO_2 bulk glasses. This was mainly explained by significant differences in the organization of the tetrahedral units TO_4 at MRO. At this structural scale, the network connectivity is expressed by a change in ring statistics favoring the formation of small rings within the sputtered thin films, leading to a denser structure and more efficient packing arrangement of TO_4. We also observed a difference within the SRO due to smaller Si–O–T inter-tetrahedral angles characterizing the network of thin films. These structural differences highlight the impact of the synthesis process. Contrary to the melt-quenched bulk glasses, the high energy ions and the fast rate of thin films deposition prevent the relaxation of their structure and favor the formation of constrained small rings. Comparing the thin film structures with those of bulk glasses, it appears that the structure of the sputtered layers is more disordered.

The impact of alumina doping on the evolution of the structure of thin films in comparison to that of bulk glasses has been brought to light. We have shown that the influence of Al_2O_3 addition on the silicate network of thin films follows the same trend as observed in bulk glasses. Specifically, aluminum atoms are incorporated into the silicate network through the formation of Si-O-Al bonds. The addition of Al_2O_3 is accompanied by an increase in the mean T-O-T angle and its distribution, which reflects an evolution of the SRO. Furthermore, Al_2O_3 doping mainly impacts the MRO, especially in the evolution of ring statistics. The addition of alumina results preferentially in a decreasing proportion of small rings. In parallel, the averaged T-T distances increase and the extent of these structural evolutions depends on the Al_2O_3 concentration. This work opens the door to the study of the structure-functional property relationships in sputtered Al_2O_3-SiO_2 thin films.

Acknowledgements
This work was supported by a grant overseen by the French National Research Agency (ANR) as part of the project “MAGI (ANR-17-CE08-0019)”.

References

1. Jiang J, Walters DM, Zhou D, Ediger MD. Substrate temperature controls molecular orientation in two-component vapor-deposited glasses. *Soft Matter*. 2016;12:3265–3270. https://doi.org/10.1039/C6SM00262E
2. Lyubimov I, Antony L, Walters DM, Rodney D, Ediger MD, de Pablo JJ. Orientational anisotropy in simulated vapor-deposited molecular glasses. *J Chem Phys*. 2015;143:094502. https://doi.org/10.1063/1.4928523
3. Diallo B, Topka KC, Puyo M, *et al.* Network hydration, ordering and composition interplay of chemical vapor deposited amorphous silica films from tetraethyl orthosilicate. *J Mater Res Technol*. 2021;13:534–547. https://doi.org/10.1016/j.jmrt.2021.04.067
4. Kimoto K, Matsui Y, Nabatame T, *et al.* Coordination and interface analysis of atomic-layer-deposition Al_2O_3 on Si(001) using energy-loss near-edge structures. *Appl Phys Lett*. 2003;83:4306–4308. https://doi.org/10.1063/1.1629397

5. Lee SK, Park SY, Yi YS, Moon J. Structure and disorder in amorphous alumina thin films: insights from high-resolution solid-state NMR. *J Phys Chem C*. 2010;114:13890–13894. https://doi.org/10.1021/jp105306r
6. Matsubara E, Kato K, Saito M, Waseda Y, Takayama S. Structural study of SiO_x amorphous thin films by the grazing incidence X-ray qcattering (GIXS) method. *Sci Rep Res Inst Tohoku Univ Ser Phys Chem Metall*. 1996;42:45–50.
7. Revesz AG, Hughes HL. The structural aspects of non-crystalline SiO_2 films on silicon: a review. *J Non-Cryst Solids*. 2003;328:48–63. https://doi.org/10.1016/S0022-3093(03)00467-8
8. Hanada T, Bessyo Y, Soga N. Elastic constants of amorphous thin films in the systems SiO_2-Al_2O_3 and $AlPO_4$-Al_2O_3. *J Non-Cryst Solids*. 1989;113:213–220. https://doi.org/10.1016/0022-3093(89)90014-8
9. Hanada T, Soga N. Coordination and bond character of silicon and aluminum ions in amorphous thin films in the system SiO_2-Al_2O_3. *J Am Ceram Soc*. 1982;65:c84–c86. https://doi.org/10.1111/j.1151-2916.1982.tb10456.x
10. Nagata K, Ogura A, Hirosawa I, Suwa T, Teramoto A, Ohmi T. Detection of short range order in SiO_2 thin-films by grazing-incidence wide and small-angle X-ray scattering. *J Appl Phys*. 2016;119:154103. https://doi.org/10.1063/1.4947053
11. Ohsaki H, Miura K, Imai A, Tada M, Aegerter MA. Structural analysis of SiO_2 gel films by high energy electron diffraction. *J Sol-Gel Sci Technol*. 1994;2:245–249. https://doi.org/10.1007/BF00486249
12. Zachariasen WH. The atomic arrangement in glass. *J Am Ceram Soc*. 1932;54:3841–3851. https://doi.org/10.1021/ja01349a006
13. Huang PY, Kurasch S, Srivastava A, *et al.* Direct imaging of a two-dimensional silica glass on graphene. *Nano Lett*. 2012;12:1081–1086. https://doi.org/10.1021/nl204423x
14. Galeener FL. Planar rings in glasses. *Solid State Commun*. 1982;44:1037–1040.
15. Meier R, Ha T-K. A theoretical study of the electronic structure of disiloxane [$(SiH_3)_2O$] and its relation to silicates. *Phys Chem Miner*. 1980;6:37–46. https://doi.org/10.1007/BF00308392
16. Grigoriev FV, Katkova EV, Sulimov AV, Sulimov VB, Tikhonravov AV. Annealing of deposited SiO_2 thin films: full-atomistic simulation results. *Opt Mater Express*. 2016;6:3960. https://doi.org/10.1364/OME.6.003960
17. Pasquarello A, Car R. Identification of Raman defect lines as signatures of ring structures in vitreous silica. *Phys Rev Lett*. 1998;80:5145–5147. https://doi.org/10.1103/PhysRevLett.80.5145
18. Rahmani A, Benoit M, Benoit C. Signature of small rings in the Raman spectra of normal and compressed amorphous silica: A combined classical and *ab initio* study. *Phys Rev B*. 2003;68:184202. https://doi.org/10.1103/PhysRevB.68.184202
19. Vollmayr K Kob, W, Binder, K. Cooling-rate in amorphous silica: a computer-simulation study. *Phys Rev B*. 1996;54:15808–15827.
20. Wang Z, Du T, Anoop Krishnan NM, Smedskjaer MM, Bauchy M. On the equivalence of vapor-deposited and melt-quenched glasses. *J Chem Phys*. 2020;152:164504. https://doi.org/10.1063/5.0006590
21. Rino JP, Ebbsjö I, Kalia RK, Nakano A, Vashishta P. Structure of rings in vitreous SiO2. *Phys Rev B*. 1993;47:3053–3062. https://doi.org/10.1103/PhysRevB.47.3053
22. Shi Y, Neuefeind J, Ma D, *et al.* Ring size distribution in silicate glasses revealed by neutron scattering first sharp diffraction peak analysis. *J Non-Cryst Solids*. 2019;516:71–81. https://doi.org/10.1016/j.jnoncrysol.2019.03.037
23. Büchner C, Lichtenstein L, Heyde M, Freund H-J. The Atomic Structure of Two-Dimensional Silica. In: Morita S, Giessibl FJ, Meyer E, Wiesendanger R, eds. *Noncontact At. Force Microsc.* Cham: Springer International Publishing; 2015:327–353. https://doi.org/10.1007/978-3-319-15588-3_16

24. Lewandowski AL, Tosoni S, Gura L, *et al.* Growth and atomic-scale characterization of ultrathin silica and germania films: The crucial role of the metal support. *Chem – Eur J*. 2021;27:1870–1885. https://doi.org/10.1002/chem.202001806
25. Ben Khemis S, Burov E, Montigaud H, Skrelic D, Gouillart E, Cormier L. Structural analysis of sputtered amorphous silica thin films: A Raman spectroscopy investigation. *Thin Solid Films*. 2021;733:138811. https://doi.org/10.1016/j.tsf.2021.138811
26. Granata M, Coillet E, Martinez V, *et al.* Correlated evolution of structure and mechanical loss of a sputtered silica film. *Phys Rev Mater*. 2018;2:053607. https://doi.org/10.1103/PhysRevMaterials.2.053607
27. Borowicz P, Latek M, Rzodkiewicz W, Łaszcz A, Czerwinski A, Ratajczak J. Deep-ultraviolet Raman investigation of silicon oxide: thin film on silicon substrate versus bulk material. *Adv Nat Sci Nanosci Nanotechnol*. 2012;3:045003. https://doi.org/10.1088/2043-6262/4/045003
28. Ponton S, Dhainaut F, Vergnes H, *et al.* Investigation of the densification mechanisms and corrosion resistance of amorphous silica films. *J Non-Cryst Solids*. 2019;515:34–41. https://doi.org/10.1016/j.jnoncrysol.2019.04.005
29. Sen PN, Thorpe MF. Phonons in AX_2 glasses: From molecular to band-like modes. *Phys Rev B*. 1977;15:4030–4038. https://doi.org/10.1103/PhysRevB.15.4030
30. Galeener FL. Band limits and the vibrational spectra of tetrahedral glasses. *Phys Rev B*. 1979;19:4292–4297. https://doi.org/10.1103/PhysRevB.19.4292
31. Weigel C, Foret M, Hehlen B, *et al.* Polarized Raman spectroscopy of v-SiO_2 under rare-gas compression. *Phys Rev B*. 2016;93:224303. https://doi.org/10.1103/PhysRevB.93.224303
32. Poulsen HF, Neuefeind J, Neumann H-B, Schneider JR, Zeidler MD. Amorphous silica studied by high energy X-ray diffraction. *J Non-Cryst Solids*. 1995;188:63–74. https://doi.org/10.1016/0022-3093(95)00095-X
33. Mauri F, Pasquarello A, Pfrommer BG, Yoon Y-G, Louie SG. Si-O-Si bond-angle distribution in vitreous silica from first-principles ^{29}Si NMR analysis. *Phys Rev B*. 2000;62:R4786–R4789. https://doi.org/10.1103/PhysRevB.62.R4786
34. McMillan PF. Flame-broiled alumina. *Nature*. 2004;430:738–738. https://doi.org/10.1038/430738a
35. Kaushik M, Leroy C, Chen Z, *et al.* Atomic-scale structure and its impact on chemical properties of aluminum oxide layers prepared by atomic layer deposition on silica. *Chem Mater*. 2021;33:3335–3348. https://doi.org/10.1021/acs.chemmater.1c00516
36. Lee SK, Lee SB, Park SY, Yi YS, Ahn CW. Structure of amorphous aluminum oxide. *Phys Rev Lett*. 2009;103:095501. https://doi.org/10.1103/PhysRevLett.103.095501
37. Shi C, Alderman OLG, Berman D, *et al.* The structure of amorphous and deeply supercooled liquid alumina. *Front Mater*. 2019;6:38. https://doi.org/10.3389/fmats.2019.00038
38. Davis S, Gutiérrez G. Structural, elastic, vibrational and electronic properties of amorphous Al_2O_3 from ab initio calculations. *J Phys Condens Matter*. 2011;23:495401.
39. Kohara S, Akola J, Patrikeev L, *et al.* Atomic and electronic structures of an extremely fragile liquid. *Nat Commun*. 2014;5:5892. https://doi.org/10.1038/ncomms6892
40. Skinner LB, Barnes AC, Salmon PS, *et al.* Joint diffraction and modeling approach to the structure of liquid alumina. *Phys Rev B*. 2013;87:024201.
41. Lee SK, Ryu S. Probing of triply coordinated oxygen in amorphous Al_2O_3. *J Phys Chem Lett*. 2018;9:150–156. https://doi.org/10.1021/acs.jpclett.7b03027
42. Lee SK, Ahn CW. Probing of 2 dimensional confinement-induced structural transitions in amorphous oxide thin film. *Sci Rep*. 2015;4:4200. https://doi.org/10.1038/srep04200
43. Sarou-Kanian V, Gleizes AN, Florian P, Samélor D, Massiot D, Vahlas C. Temperature-dependent 4-, 5- and 6-fold coordination of aluminum in MOCVD-grown amorphous alumina films: a very high field ^{27}Al-NMR study. *J Phys Chem C*.

2013;117:21965–21971. https://doi.org/10.1021/jp4077504
44. Cormier L. Glasses: Aluminosilicates. *Encycl. Mater. Tech. Ceram. Glas.* Elsevier; 2021:496–518. https://doi.org/10.1016/B978-0-12-818542-1.00076-X
45. Neuville DR, Cormier L, Montouillout V, *et al.* Structure of Mg- and Mg/Ca aluminosilicate glasses: ^{27}Al NMR and Raman spectroscopy investigations. *Am Min*. 2008;93:1721–1731. https://doi.org/10.2138/am.2008.2867
46. Neuville DR, Cormier L, Massiot D. Al coordination and speciation in calcium aluminosilicate glasses: effects of composition determined by ^{27}Al MQ-MAS NMR and Raman spectroscopy. *Chem Geol*. 2006;229:173–185. https://doi.org/10.1016/j.chemgeo.2006.01.019
47. Allwardt JR, Stebbins JF, Schmidt BC, Frost DJ, Withers AC, Hirschmann MM. Aluminum coordination and the densification of high-pressure aluminosilicate glasses. *Am Miner*. 2005;90:1218–1222.
48. Lee SK. Effect of pressure on structure of oxide glasses at high pressure: Insights from solid-state NMR of quadrupolar nuclides. *Solid State Nucl Magn Reson*. 2010;38:45–57. https://doi.org/10.1016/j.ssnmr.2010.10.002
49. Yarger JL Smith, KH, Nieman, RA, Diefenbacher, J, Wolf, GH, Poe, BT, McMillan, PF. Al coordination changes in high-pressure aluminosilicate liquids. *Science*. 1995;270:1964–1967.
50. Fujiyama H, Sumomogi T, Nakamura M. Effect of O_2 gas partial pressure on mechanical properties of Al_2O_3 films deposited by inductively coupled plasma-assisted radio frequency magnetron sputtering. *J Vac Sci Technol Vac Surf Films*. 2012;30:051511. https://doi.org/10.1116/1.4746013
51. Young MJ, Bedford NM, Yanguas-Gil A, *et al.* Probing the atomic-scale structure of amorphous aluminum oxide grown by atomic layer deposition. *ACS Appl Mater Interfaces*. 2020;12:22804–22814. https://doi.org/10.1021/acsami.0c01905
52. Cormier L, Neuville DR, Calas G. Structure and properties of low-silica calcium aluminosilicate glasses. *J Non-Cryst Solids*. 2000;274:110–114. https://doi.org/10.1016/S0022-3093(00)00209-X
53. Morikawa H, Miwa S-I, Miyake M, Marumo F, Sata T. Structural analysis of SiO_2-Al_2O_3 glasses. *J Am Ceram Soc*. 1982;65:78–81. https://doi.org/10.1111/j.1151-2916.1982.tb10361.x
54. Okuno M, Zotov N, Schmücker M, Schneider H. Structure of SiO_2-Al_2O_3 glasses: Combined X-ray diffraction, IR and Raman studies. *J Non-Cryst Solids*. 2005;351:1032–1038. https://doi.org/10.1016/j.jnoncrysol.2005.01.014
55. Poe BT, McMillan PF, Angell CA, Sato RK. Al and Si coordination in SiO_2-Al_2O_3 glasses and liquids - A study by NMR and IR spectroscopy and MD simulations. *Chem Geol*. 1992;96:333–349. https://doi.org/10.1016/0009-2541(92)90063-b
56. Ren J, Zhang L, Eckert H. Medium-range order in sol-gel prepared Al_2O_3-SiO_2 glasses: New results from solid-state NMR. *J Phys Chem C*. 2014;118:4906–4917. https://doi.org/10.1021/jp412774h
57. Risbud SH, Kirkpatrick RJ, Taglialavore AP, Montez B. Solid-state NMR evidence of 4-, 5, and 6-fold aluminum sites in roller-quenched SiO_2-$A1_2O_3$ glasses. *J Am Ceram Soc*. 1987;70:C-10-C–12. https://doi.org/10.1111/j.1151-2916.1987.tb04859.x
58. Sato RK, McMillan PF, Dennison P, Dupree R. High-resolution ^{27}Al and ^{29}Si MAS NMR investigation of SiO_2-Al_2O_3 glasses. *J Phys Chem*. 1991;95:4483–4489.
59. Sen S, Youngman RE. High-resolution multinuclear NMR structural study of binary aluminosilicate and other related glasses. *J Phys Chem B*. 2004;108:7557–7564. https://doi.org/10.1021/jp031348u
60. Weber R, Sen S, Youngman RE, Hart RT, Benmore CJ. Structure of high alumina content Al_2O_3-SiO_2 composition glasses. *J Phys Chem B*. 2008;112:16726–16733. https://doi.org/10.1021/jp807964u

61. Wilding MC, Benmore CJ, Weber JKR. High-energy X-ray diffraction from aluminosilicate liquids. *J Phys Chem B*. 2010;114:5742–5746. https://doi.org/10.1021/jp907587e
62. Ando MF, Benzine O, Pan Z, *et al.* Boson peak, heterogeneity and intermediate-range order in binary SiO_2-Al_2O_3 glasses. *Sci Rep*. 2018;8:5394. https://doi.org/10.1038/s41598-018-23574-1
63. Le Cornec D, Cormier L, Galoisy L, *et al.* Molecular structure of amorphous slags: An experimental and numerical approach. *J Non-Cryst Solids*. 2021;556:120444. https://doi.org/10.1016/j.jnoncrysol.2020.120444
64. Juhás P, Davis T, Farrow CL, Billinge SJL. PDFgetX3 : a rapid and highly automatable program for processing powder diffraction data into total scattering pair distribution functions. *J Appl Crystallogr*. 2013;46:560–566. https://doi.org/10.1107/S0021889813005190
65. Ohira I, Murakami M, Kohara S, Ohara K, Ohtani E. Ultrahigh-pressure acoustic wave velocities of SiO2-Al2O3 glasses up to 200 GPa. *Prog Earth Planet Sci*. 2016;3:18. https://doi.org/10.1186/s40645-016-0097-2
66. Rosales-Sosa GA, Masuno A, Higo Y, Inoue H. Crack-resistant Al_2O_3-SiO_2 glasses. *Sci Rep*. 2016;6:23620. https://doi.org/10.1038/srep23620
67. Hehlen B, Neuville DR, Kilymis D, Ispas S. Bimodal distribution of Si–O–Si angles in sodo-silicate glasses. *J Non-Cryst Solids*. 2017;469:39–44. https://doi.org/10.1016/j.jnoncrysol.2017.04.009
68. Shibata N, Horigudhi M, Edahiro T. Raman spectra of binary high-silica glasses and fibers containing GeO_2, P_2O_5 and B_2O_3. *J Non-Cryst Solids*. 1981;45:115–126. https://doi.org/10.1016/0022-3093(81)90096-X
69. Wang Y, Wei S, Cicconi MR, *et al.* Femtosecond laser direct writing in SiO_2-Al_2O_3 binary glasses and thermal stability of Type II permanent modifications. *J Am Ceram Soc*. 2020;103:4286–4294. https://doi.org/10.1111/jace.17164
70. McMillan PG, Piriou B. The structures and vibrational spectra of crystals and glasses in the silica-alumina system. *J Non-Cryst Solids*. 1982;53:279–298. https://doi.org/10.1016/0022-3093(82)90086-2
71. Walrafen GE, Krishnan PN. Model analysis of the Raman spectrum from fused silica optical fibers. *Appl Opt*. 1982;21:359. https://doi.org/10.1364/AO.21.000359
72. Sharma SK, Mammone JF, Nicol MF. Raman investigation of ring configurations in vitreous silica. *Nature*. 1981;292:140–141. https://doi.org/10.1038/292140a0
73. Barnini A. Mise au point et caractérisation de nouvelles compositions de verres de silice dopée ytterbium par méthode plasma (SPCVD) pour application en tant que fibre laser. PhD Thesis; Université Pierre et Marie Curie - Paris VI; Paris; 2017
74. Taylor M, Brown GE. Structure of mineral glasses—I. The feldspar glasses $NaAlSi_3O_8$, $KAlSi_3O_8$, $CaAl_2Si_2O_8$. *Geochim Cosmochim Acta*. 1979;43:61–75. https://doi.org/10.1016/0016-7037(79)90047-4
75. Zotov N, Dimitrov V, Yanev Y. X-ray radial distribution function analysis of acid volcanic glasses from the Eastern Rhodopes, Bulgaria. *Phys Chem Miner*. 1989;16:774–778.
76. Whittaker EJW, Muntus R. Ionic radii for use in geochemistry. *Geochim Cosmochim Acta*. 1970;34:945–956. https://doi.org/10.1016/0016-7037(70)90077-3
77. Cormier L, Ghaleb D, Neuville DR, Delaye J-M, Calas G. Chemical dependence of network topology of calcium aluminosilicate glasses: a computer simulation study. *J Non-Cryst Solids*. 2003;332:255–270. https://doi.org/10.1016/j.jnoncrysol.2003.09.012
78. Majérus O, Cormier L, Neuville DR, Galoisy L, Calas G. The structure of SiO_2-GeO_2 glasses: A spectroscopic study. *J Non-Cryst Solids*. 2008;354:2004–2009. https://doi.org/10.1016/j.jnoncrysol.2007.11.004
79. Brower KL. Electron paramagnetic resonance of Al E_1' centers in vitreous silica. *Phys*

Rev B. 1979;20:1799–1811. https://doi.org/10.1103/PhysRevB.20.1799
80. Brower KL. Structural and trapping characteristics of a new Al defect in vitreous silica. *Phys Rev Lett*. 1978;41:879–881. https://doi.org/10.1103/PhysRevLett.41.879
81. Momida H, Hamada T, Takagi Y, Yamamoto T, Uda T, Ohno T. Theoretical study on dielectric response of amorphous alumina. *Phys Rev B*. 2006;73:054108. https://doi.org/10.1103/PhysRevB.73.054108
82. Song W, Li X, Wang B, *et al.* Atomic picture of structural relaxation in silicate glasses. *Appl Phys Lett*. 2019;114:233703. https://doi.org/10.1063/1.5095529
83. D'Heurle FM, Harper JME. Note on the origin of intrinsic stresses in films deposited via evaporation and sputtering. *Thin Solid Films*. 1989;171:81–92. https://doi.org/10.1016/0040-6090(89)90035-7
84. Thornton JA, Hoffman DW. Internal stresses in titanium, nickel, molybdenum, and tantalum films deposited by cylindrical magnetron sputtering. *J Vac Sci Technol*. 1977;14:164–168. https://doi.org/10.1116/1.569113
85. Debelle A. Contraintes, microstructure et sollicitation sous irradiation aux ions de films minces élaborés par pulvérisation ionique: modélisation et application à l'étude des effets interfaciaux dans des multicouches métalliques. PhD Thesis; Université de Poitiers; Popitiers; 2005
86. Cohen HM, Roy R. Reply to "Comments on'Effects of ultrahigh pressures on glass'." *J Am Ceram Soc*. 1962;45:398–399. https://doi.org/10.1111/j.1151-2916.1962.tb11178.x
87. Mackenzie JD. High-Pressure effects on oxide glasses: I, Densification in rigid state. *J Am Ceram Soc*. 1963;46:461–470. https://doi.org/10.1111/j.1151-2916.1963.tb13776.x
88. Vandembroucq D, Deschamps T, Coussa C, *et al.* Density hardening plasticity and mechanical ageing of silica glass under pressure: a Raman spectroscopic study. *J Phys Condens Matter*. 2008;20:485221. https://doi.org/10.1088/0953-8984/20/48/485221
89. Gerbig YB, Michaels CA. In-situ Raman spectroscopic measurements of the deformation region in indented glasses. *J Non-Cryst Solids*. 2020;530:119828. https://doi.org/10.1016/j.jnoncrysol.2019.119828
90. Barthel E, Keryvin V, Rosales-Sosa G, Kermouche G. Indentation cracking in silicate glasses is directed by shear flow, not by densification. *Acta Mater*. 2020;194:473–481. https://doi.org/10.1016/j.actamat.2020.05.011
91. Martinet C, Heili M, Martinez V, *et al.* Highlighting the impact of shear strain on the SiO_2 glass structure: From experiments to atomistic simulations. *J Non-Cryst Solids*. 2020;533:119898. https://doi.org/10.1016/j.jnoncrysol.2020.119898
92. Shcheblanov NS, Mantisi B, Umari P, Tanguy A. Detailed analysis of plastic shear in the Raman spectra of SiO_2 glass. *J Non-Cryst Solids*. 2015;428:6–19. https://doi.org/10.1016/j.jnoncrysol.2015.07.035
93. Hoffman DW, Thornton JA. The compressive stress transition in Al, V, Zr, Nb and W metal films sputtered at low working pressures. *Thin Solid Films*. 1977;45:387–396. https://doi.org/10.1016/0040-6090(77)90276-0
94. Ma X, Zhang J, Cai W, *et al.* A Sputtered silicon oxide electrolyte for high-performance thin-film transistors. *Sci Rep*. 2017;7:809. https://doi.org/10.1038/s41598-017-00939-6

Supplementary Information

Comparative Structural Study of Al_2O_3-SiO_2 Glasses and Amorphous Thin Films

Sirine Ben Khemis[1,2], Laurent Cormier[1], Ekaterina Burov[2], Hervé Montigaud[2], Benoit Baptiste[1], Sophie Nowak[3]

[1] *Sorbonne Université, Muséum National d'Histoire Naturelle, UMR CNRS 7590, IRD, Institut de Minéralogie, de Physique des Matériaux et de Cosmochimie, IMPMC, 75005 Paris, France*

[2] *Surface du Verre et Interface (UMR 125), CNRS/Saint-Gobain Research Paris, 93300 Aubervilliers, France*

[3] *Université Paris Cité, UMR CNRS 7086, ITODYS, 75013 Paris, France*

❖ **Experimental parameters of the deposition of the different films to prepare the "reflective mask substrate"**

TABLE S1 Parameters used in direct current (DC) magnetron sputtering of SiO_2, Ag, NiCr and AZO.

Target	Si	Ag	NiCr	AZO
Power (W)	3000	500	500	1300
Pressure (Pa)	0.2	0.8	0.2	0.2
Ar flow (sccm)	20	150	50	40
O_2 flow (sccm)	24	0	0	0

❖ **Determination of the density of thin layers by X-ray reflectivity measurements**

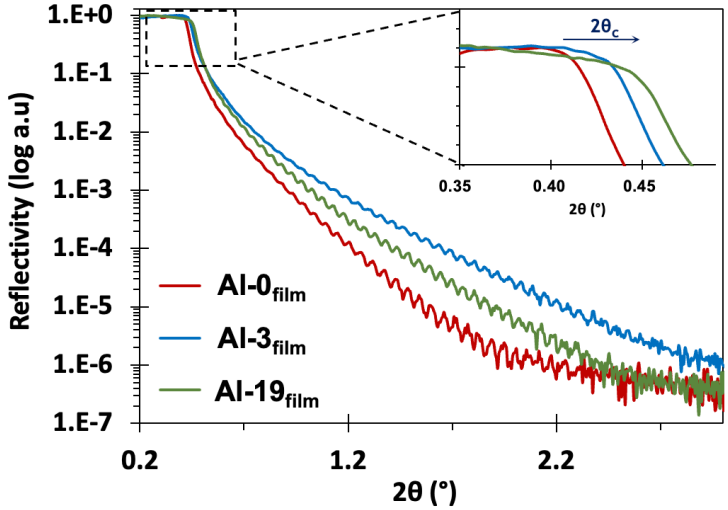

FIGURE S1 Reflectivity spectra obtained on SiO_2-Al_2O_3 thin layers (150 nm) with different Al_2O_3 contents and deposited on a glass substrate. The insert emphasizes the shift of the critical angle θ_c as a function of the alumina content.

Figure S1 shows the X-ray reflectivity curves. The insert in figure S1 shows the plateau region limited by the critical angle θ_c of total reflection. This angle is related to the electronic density of the material. The shift of θ_c towards high angle values reflects an increase in the electronic density of the thin film layer as the Al_2O_3 content increases. In order to determine the density, an analysis of the spectra was carried out using the simulation software «X'Pert Reflectivity». The simulated spectra are shown in Figure S2. By adjusting the model parameters, we obtain the structural parameters of each layer (thickness, roughness and density).

Figure S2 shows the experimental (blue) and simulated (red) reflectivity curves that are obtained by adjusting the least squares with the segmented fit algorithm. Table S2 summarizes the structural parameters of thin silica layers with different alumina contents.

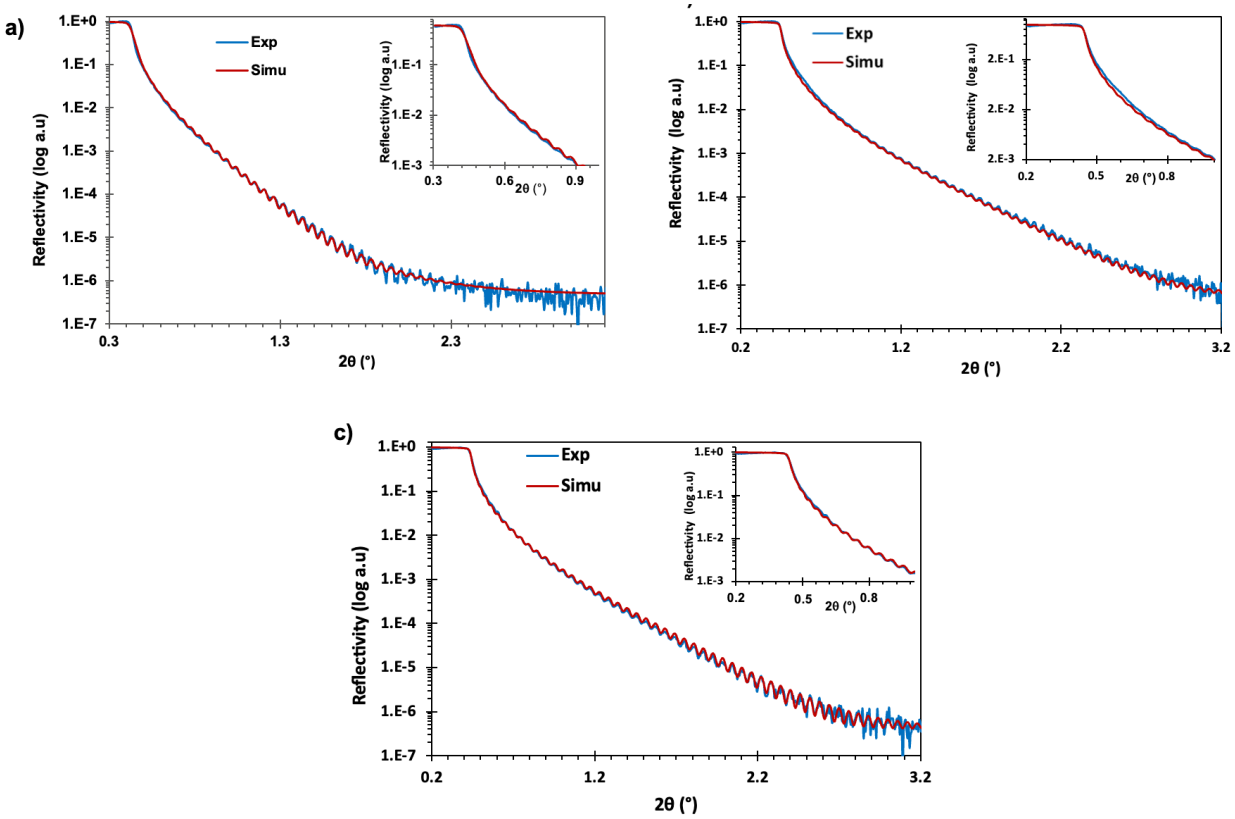

FIGURE S2 Experimental (blue) and simulated (red) reflectivity curves for SiO_2-Al_2O_3 thin film layers of silica (150 nm) containing different alumina contents: a) 0 mol% Al_2O_3, named Al-0_{film} (b) 3 mol% Al_2O_3, named Al-3_{film} and (c) 18.6 mol% Al_2O_3, named Al-19_{film}.

TABLE S2 Structural parameters of the silica layers (thickness, roughness and density) doped with different alumina contents.

	Thickness (nm)	Density (g.cm^{-3})	Roughness (nm)
Al-0$_{film}$	150	2.35	1.8
Al-3$_{film}$	151	2.38	1.0
Al-19$_{film}$	159	2.50	1.33

❖ **Fitting of the Raman spectra**

Raman data were acquired between 100-1350 cm^{-1}. At low frequency, a peak called Boson peak is present with an intensity that varies with the temperature as the Bose-Einstein factor. Its asymmetric shape can be represented by a log-normal law (Pang, 1992):

$$I_{BP} = \frac{A}{\sqrt{2\pi}\sigma\omega} exp\left(\frac{-\left(ln\frac{\omega}{x_{BP}}\right)}{2\sigma^2}\right)$$

with A an amplitude factor, x_{BP} the position of the Boson peak and σ the standard deviation determining the width. We used this function to subtract this contribution that extends over all the spectrum though the spectral range is limited at low frequencies. We then normalized by the area over the spectral range 100-1300 cm^{-1} and to the maximum intensity.

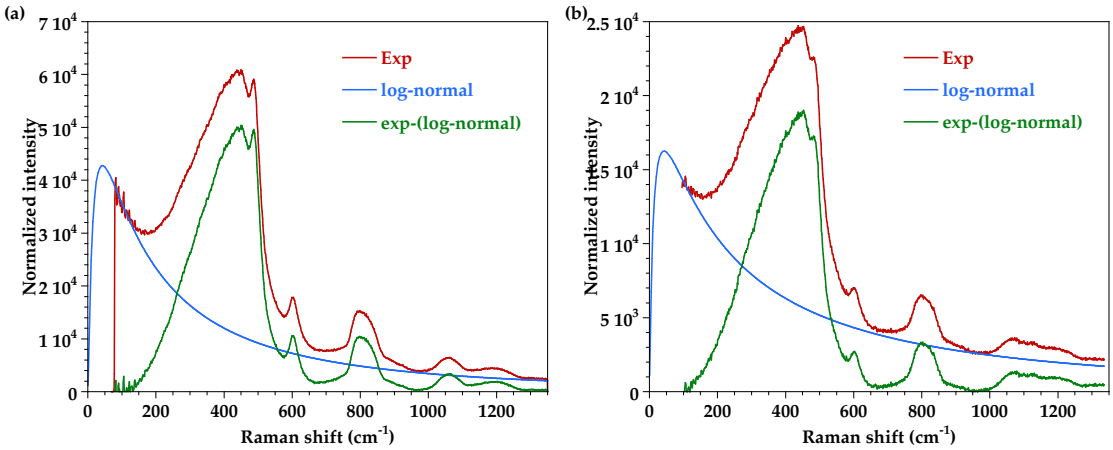

FIGURE S3 Correction of the (a) Al-1_{bulk} and (b) Al-5_{bulk} glasses.

Then the Raman spectra are fitted using six gaussian functions. Figure S3 shows the fitting results of the Raman spectra for the SiO2-Al2O3 bulk glasses. Data fitting was executed employing a nonlinear optimization method, aimed at minimizing the sum of squared residuals. All datasets were processed consistently using homemade Python routines. The Raman fit spectrum employed pseudo-Voigt functions, each characterized by four parameters: intensity, position, width at half maximum and Gaussian/Lorentzian ratio. Initial parameters for the pseudo-Voigt profiles were set based on literature values and used as a starting point for the fit. Subsequently, the Levenberg-Marquardt algorithm was applied iteratively to adjust the initial parameters, aiming to minimize the residual error between the modeled and measured Raman spectra. Throughout the fitting procedure, all parameters were left unconstrained, except for fixing the number of pseudo-Voigt bands.

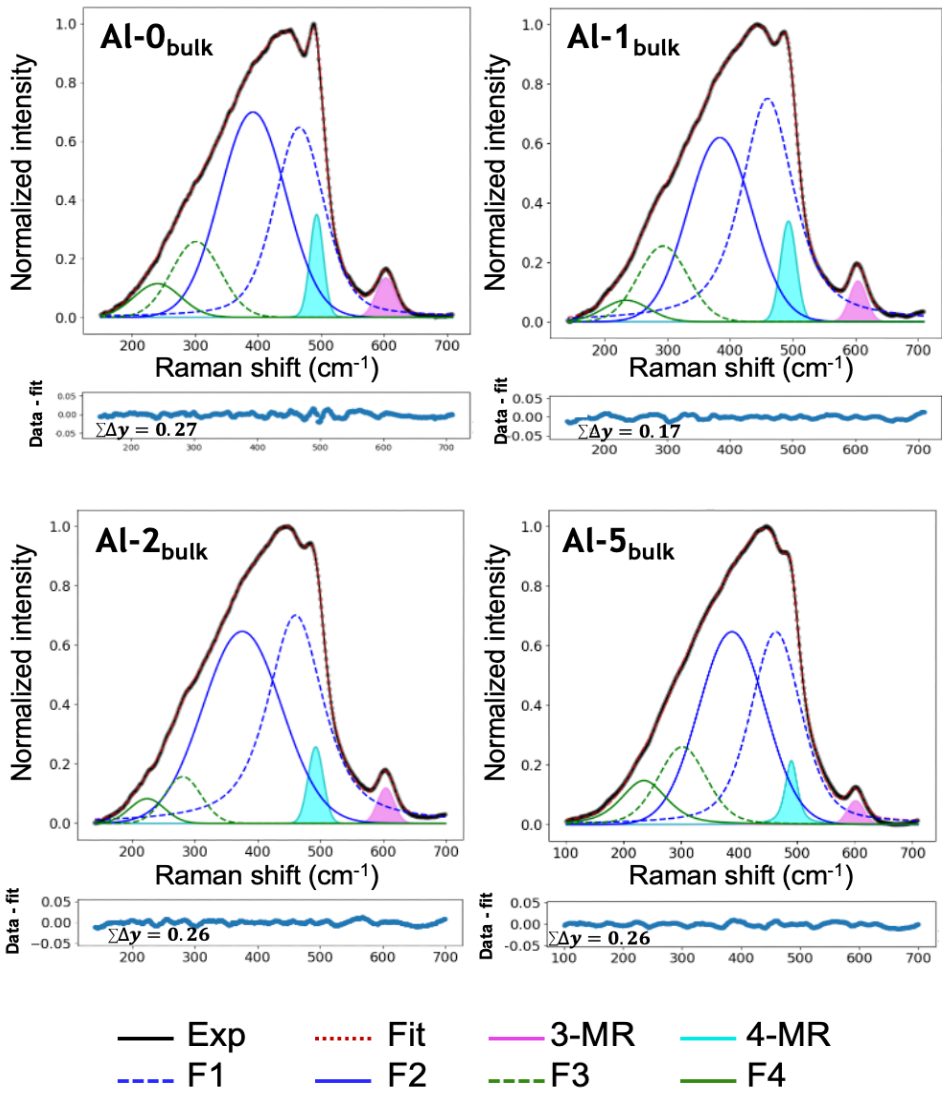

FIGURE S4 Fit of Raman spectra of SiO_2-Al_2O_3 bulk glasses with different alumina contents (0, 1, 2, 5 mol% Al_2O_3).

❖ **Pair distribution function for SiO_2-Al_2O_3 glasses**

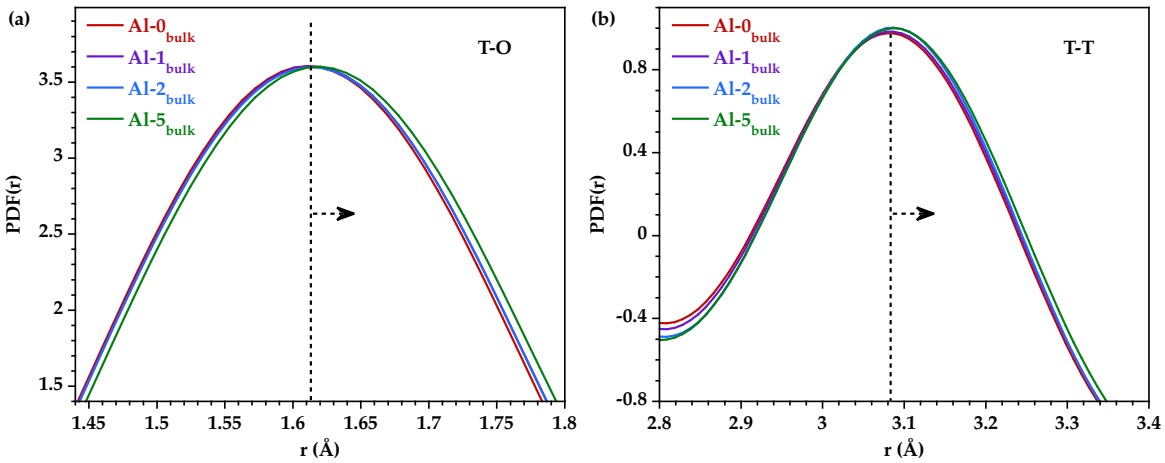

FIGURE S5 Evolution of the (a) T-O and (b) T-T pairs in the PDF functions of bulk glasses.

❖ **GI-XRD diffractogram of Al-19$_{film}$ deposited on a glass substrate**

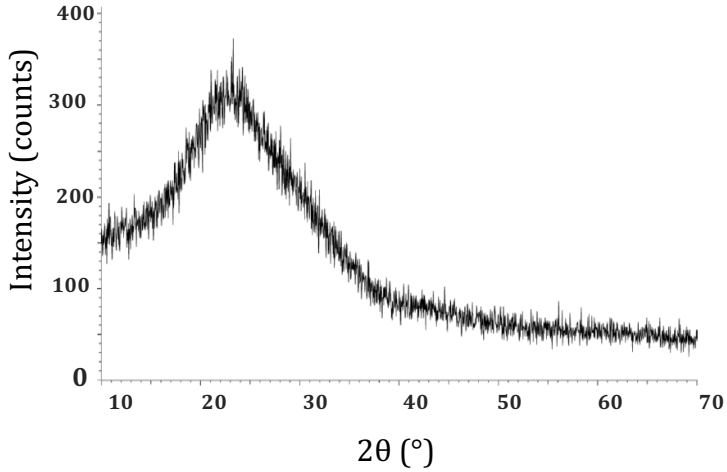

FIGURE S6 GI-XRD patterns of Al-19$_{film}$ deposited directly on a glass substrate.

❖ **Pair distribution function for SiO_2-Al_2O_3 thin films**

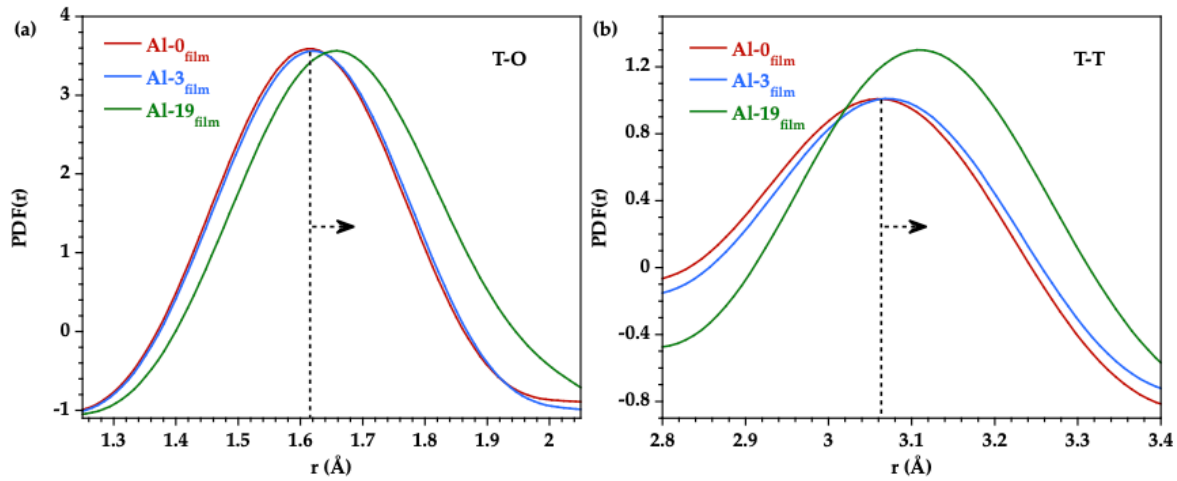

FIGURE S7 Evolution of the (a) T-O and (b) T-T pairs in the PDF functions of thin films.

❖ Packing density of SiO_2-Al_2O_3 thin films and glasses

The packing density is calculated. From the density values in figure 1, following Makishima and Mackenzie .(Makishima, A., et J.D. Mackenzie. « Direct Calculation of Young's Modulus of Glass ». *Journal of Non-Crystalline Solids* 12 (1973) 35-45 https://doi.org/10.1016/0022-3093(73)90053-7).

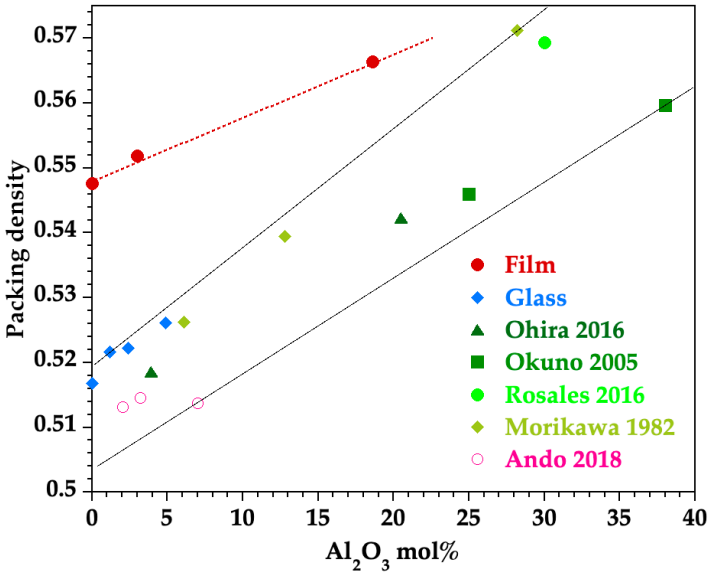

FIGURE S8 Packing density of SiO_2-Al_2O_3 thin films and glasses